Synthesis of orthorhombic rare-earth manganite thin films by a novel chemical solution route

Y. Romaguera-Barcelay · J. Agostinho Moreira ·
G. González-Aguilar · A. Almeida · J. P. Araujo ·
J. Pérez de la Cruz

Abstract A novel and general chemical solution route for processing high-quality transition metal and rare-earth orthorhombic manganite thin films on Pt(111)/Ti/SiO$_2$/Si substrates was reported. The precursor solutions decomposition process of the manganites was studied by TG and DTA techniques, showing the formation of the phase above 650°C in LaMnO$_3$ and 750°C in both EuMnO$_3$ and DyMnO$_3$ thin films. X-ray diffraction and Raman spectroscopic analysis reveal the formation of a pure orthorhombic structure, with a space group *Pbnm*, in LaMnO$_3$, EuMnO$_3$ and DyMnO$_3$ thin films annealed at temperatures above **the TG** phase formation temperature **observed**. Microstructure and grain morphology of the films were analyzed by SEM and AFM techniques, showing a progressive improvement of the films structures with the increase of the annealing temperature. The temperature dependence of the magnetic response of the LaMnO$_3$, EuMnO$_3$ and DyMnO$_3$ thin films show typical transition temperatures, compared with those reported for lanthanum, europium and dysprosium manganite single crystals and ceramics.

Keywords Orthorhombic rare-earth manganites · Thin films · Sol–gel route

Y. Romaguera-Barcelay · G. González-Aguilar ·
J. Pérez de la Cruz (✉)
INESCPorto,
Rua do Campo Alegre, 687,
4169-007 Porto, Portugal
e-mail: jcruz@inescporto.pt

Y. Romaguera-Barcelay · J. A. Moreira · A. Almeida · J. P. Araujo
Departamento de Física da Faculdade de Ciências da
Universidade do Porto, IFIMUP and IN- Institute of Nanoscience and Nanotechnology,
Rua do Campo Alegre, 687,
4169-007 Porto, Portugal

1 Introduction

Transition metal and rare-earth manganites, with general formula RMnO$_3$, (R = rare-earth or transition metal ion) have attracted a lot of attention in the scientific community, due to their large variety of physical properties, as they can be dielectrics, metals, ferro-/antiferromagnetics, multiferroics, magnetoelectrics, magnetocaloric or giant magnetoresistive materials [1–7]. At room temperature, these materials crystallize into two types of structures [8–12]. For instance, RMnO$_3$, with *R* = Bi, La, Pr, Nd, Sm, Eu, Gd and Dy, exhibit orthorhombic structure with the *Pbnm* space group, while RMnO$_3$ with *R* = Sc, In, Yb, Lu and Er, crystallize in a hexagonal lattice, described by the *P6$_3$cm* space group [13–20]. Other manganites, such as YMnO$_3$ and HoMnO$_3$, are located at the morphotropic phase boundary, and have been reported as either hexagonal or orthorhombic, depending on the processing method used in their preparation [21–24].

Transition metal and rare-earth manganites have been extensively studied in the single crystal form, processed by floating zone method [25, 26], as well as polycrystalline samples, processed by conventional ceramic or sol–gel methods [27, 28], and thin films, prepared by several deposition techniques, such as pulsed laser deposition [29, 30], RF sputtering or RF magnetron sputtering [15, 31–33], molecular beam epitaxy [34, 35], metal-organic chemical vapor deposition [36], and chemical solution deposition [22, 37–41]. Among these methods, chemical solution deposition is one of the more promising techniques, because it provides higher composition control, lower processing temperatures, shorter fabrication time, and relative low cost [41]. It has been reported several chemical solution routes for processing transition metal

and rare-earth manganite thin films, i.e., YMnO$_3$ [22, 29, 31–34, 37–43], GdMnO$_3$ [13, 14, 17], BiMnO$_3$ [5, 17], DyMnO$_3$ [13, 17] and LaMnO$_3$ [44, 45]. However, it has been not reported a general chemical solution route for processing rare-earth and transition metal manganite thin films yet.

In this work, a novel chemical solution route suitable for processing a large variety of high-quality rare-earth and transition metal manganite thin films is reported. A complete characterization of the precursor solutions was carried out by Raman spectroscopy. Both precursor solutions decomposition process and phase formation temperature were also studied. A detailed analysis of the crystal structure, microstructure, morphology and roughness was carried out by standard and grazing angle X-ray diffractometries, scanning electron microscopy and atomic force microscopy. In order to determine the magnetic response of the as-prepared films, the induced magnetization was studied as a function of the temperature, in the 5–300 K range, and the results compared with those previously reported for single crystals and ceramics.

Although a wide set of orthorhombic rare-earth manganites was produced, in this work we only report the results concerning to LaMnO$_3$, EuMnO$_3$ and DyMnO$_3$ thin films, as they are representative members of the most relevant sets of the manganite family.

In the rare-earth manganite physics, the parent compound, LaMnO$_3$, reveals a particular importance. It is an antiferromagnetic insulator in which a C-type orbital ordering is established, owing to a cooperative Janh-Teller effect, breaking the degeneracy of the electronic configuration of the Mn^{3+} ion. This particular orbital ordering is responsible for the A-type magnetic structure, observed below 140 K in both single crystals and ceramics or below 160 K in thin films [46–50].

DyMnO$_3$ is a typical example of spiral spin-driven ferroelectric, exhibiting an incommensurate antiferromagnetic ordering below the Néel temperature, $T_N = 40$ K, and a lock-in phase transition below the Curie temperature, $T_c = 19$ K [4, 17]. The ferroelectric order, with spontaneous polarization along the c-axis, occurs below T_c. The ordering of the Dy^{3+} magnetic momenta occurs below 10 K [10].

EuMnO$_3$ is located at the boundary between the non-magnetoelectric and magnetoelectric rare-earth manganites. On decreasing temperature, EuMnO$_3$ undergoes successive magnetic phase transitions from the collinear sinusoidal state below 50 K to the layered A-type antiferromagnetic phase below 46 K [51, 52]. Recently, it has been observed that an electric polarization along the a-axis is induced under rather high magnetic fields (H>20 T) applied along the b-axis [53, 54].

2 Experimental procedure

2.1 Precursor solution and films preparation

LaMnO$_3$, EuMnO$_3$, and DyMnO$_3$ precursor solutions were prepared as follows: lanthanum acetate hydrated ((CH$_3$CO$_2$)$_3$La.xH$_2$O), dysprosium (III) nitrate hydrated ((NO$_3$)$_3$Dy•xH$_2$O), both 99.9% purity, and europium (III) acetate hydrated ((CH$_3$CO$_2$)$_3$Eu•xH$_2$O) 99.99% pure (supplied by *Aldrich*) were previously dissolved at 50°C, in a glacial acetic acid (CH$_2$CO$_2$H) and nitric acid (HNO$_3$) 2:1 molar ratio mixture, during 24 h. Once the lanthanide precursors were dissolved, a stoichiometric molar content of manganese (II) acetate tetrahydrate ((CH$_3$COO)$_2$Mn•x4H$_2$O), 99.99% pure (supplied by *Merck*), was added. The resulting solutions were stabilized with pure 2-methoxyethanol, in a solvent (2:1:6) molar ratio (CH$_2$CO$_2$H/HNO$_3$/CH$_2$OCH$_2$CH$_2$OH). Finally, a 0.2 molar concentration was achieved in all the precursor solutions.

The rare-earth manganite precursor solutions were deposited onto Pt(111)/TiO$_2$/SiO$_2$/Si substrates, using a Laurell WS-400-6NPP automatic spin-coater. Each individual layer was deposited at 3000 rpm during 60 seconds, dried at 80 °C for a minute and pre-sintered at 400°C during 10 min. This process was repeated 5 times in order to obtain films with ~240 nm of thickness. Afterward, the films processed from each type of solution were separately annealed at 650°C, 700°C, 750°C, 800°C and 850°C for an hour, followed by a quenching at 25°C in air atmosphere.

2.2 Experimental techniques

Unpolarized Raman spectra were obtained by a T64000 Jobin-Yvon triple spectrometer, equipped with a liquid-nitrogen-cooled charge coupled device. The 514.5 nm polarized line of an Ar+ laser was used for excitation, with an incident power of about 10 mW impinging on the sample, in order to avoid local heating. The spectral slit width was ~1.5 cm^{-1}. These conditions were maintained during all the experiments, which were performed at room temperature. In order to carry out these measurements, the precursor solutions were dropped inside an amorphous cell, while Raman scattered radiation in the 200 cm^{-1}–4000 cm^{-1} frequency range was recorded. Instead, the unpolarized Raman studies of the films were carried out in the 200 cm^{-1}–800 cm^{-1} frequency range, with the samples situated in a micro-Raman set-up.

Thermogravimetric (TG) and differential thermogravimetric analysis (DTA) were carried out in the LaMnO$_3$, EuMnO$_3$, and DyMnO$_3$ solutions, using a Seteram Labsys TG-DTA/DSC analyzer. In order to perform the TG and DTA measurements, the solutions were dried at 100°C during 48 h, forming the so-called *dry* solutions. Afterward,

they were heated, in air atmosphere, at a rate of 10°C/min from room temperature up to 1000°C.

Standard and grazing angle X-ray diffraction patterns of the films were recorded by a Phillips diffractometer, with Cu k_α radiation. The measurements were performed from 20º to 80º (2θ) in continuous (0.01º/s) and step (0.01º/10 s) modes, respectively.

Scanning electron microscopy (SEM) images were recorded by a Jeol field emission scanning electron microscope, working at 15 kV@11 mA. The morphology of the films surface was analyzed by atomic force microscopy (AFM) technique, using a Veeco Multimode NanoScope IVa, working in tapping mode.

The induced specific magnetization measurements were performed using a commercial superconducting quantum interference SQUID magnetometer. After previous cooling down to 4 K under zero (zero field cooled—ZFC) and 100 Oe applied magnetic field (field cooled—FC), the measurements were carried out in heating run from 5 K— 300 K using a DC driving magnetic field of 100 Oe.

3 Results and discussion

3.1 Solution characterization

Figure 1(a), (b) and (c) show the Raman spectra of LaMnO₃, EuMnO₃ and DyMnO₃ precursor solutions, respectively. In order to assign the bands observed in the Raman spectra of the precursor solutions, we also studied the Raman spectra of pure 2-methoxyethanol, acetic acid and 20% aqueous solution of nitric acid. The observed
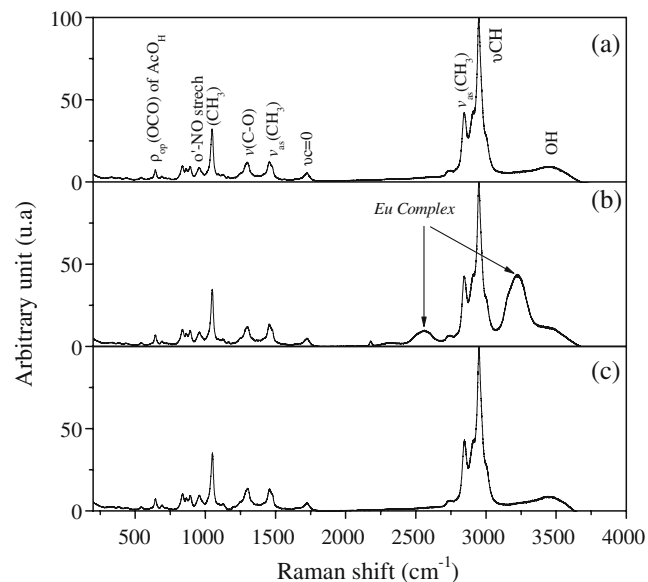
Raman spectra were compared with those previously published [55–57]. Based on the relevant published data, we have assigned the Raman bands observed in the solvent spectra, which are summarized in Table 1.

The spectral signatures of both LaMnO₃ and DyMnO₃ Raman spectra are rather similar. Their main bands correlate very well with those arising from the solvents, namely: the alcohol OH stretching mode at 3440 cm⁻¹, the C-H symmetric and asymmetric stretching modes in the 2950 cm⁻¹–3050 cm⁻¹ region, the stretching mode of the carboxylic group at 1740 cm⁻¹, and the methylenic rocking and twist modes at 1480 cm⁻¹ and 1040 cm⁻¹, respectively. The similar spectral signatures of the solvents and precursor solutions of both LaMnO₃ and DyMnO₃, provide evidence for the weak interactions between the precursor cations and solvents. However, the high frequency Raman spectrum of the EuMnO₃ precursor solution exhibits several bands, which cannot be assigned to any band arising from the solvents. It is well known that the europium ion could easily form complex with organic molecules [58–60]. As the 2-methoxyethanol molecule has two active oxygen groups, it is likely that those additional Raman bands coming from the formation of europium/2-methoxyethanol complex. Further experiments should be carried out in order to clarify this statement.

Figure 2 shows the TG-DTA curves of the prepared precursor solutions. The *dry* solution decomposition process includes three main steps: (*i*) solvent evaporation, (*ii*) calcination and (*iii*) phase formation. In the evaporation step, a weight loss of ~20% was archived in all of the samples, in good correlation with the DTA endothermic peaks. This weight loss corresponds to the complete solvent and constitutional water evaporation. Moreover, the evaporation and/or decomposition of the remaining acetic acid might also take place in this step. This step is followed by a major weigh loss between 20–40%, extending from 200°C up to 400°C, in agreement with the wide DTA endothermic peak observed around 300°C. In this temperature range, the decomposition of the organic materials into carbonates should take place [43, 61, 62]. The organic cation carbonization can be considered as the major competition reaction during the organic material decomposition, due to the oxidation of the organic compounds in air [43, 61, 62]. Minor weight loss occurs in the 400°C–600°C temperature range (~5%), which can be associated with the decomposition of some carbonate species into lanthanum, europium, dysprosium and manganese oxy-carbonates. In the third step, which takes place above 600°C, there is a significant weight loss of 1–2%, relatively to the initial weight of the *dry* solutions, which is associated with the perovskite phase formation. Although, the temperature interval of the steps depends on each material, the profile of the TG-DTA

Fig. 1 Raman spectra of: (**a**) LaMnO₃, (**b**) EuMnO₃ and (**c**) DyMnO₃ precursor solutions, recorded at room temperature

Table 1 Raman frequency modes of the **solvents** used in the chemical solution preparation

Frequency mode	Frequency (cm^{-1})	Type of solvent
Skeletal mode [a]	376	2-Methoxyethanol
$\gamma(OH)$ [a]	433	2-Methoxyethanol
CH3 [c]	470	Acetic acid
$\Delta(CCO)$ [a]	542	2-Methoxyethanol
CCO [c]	604, 624	Acetic acid
O'-NO2 bending [b]	641	Nitric acid
NO2 bending [c]	692	Nitric acid
$\gamma(CH2)$ [a]	836	2-Methoxyethanol
$v[C\_C]$ [a]	894	2-Methoxyethanol
Stretching C-C [c]	900	Acetic acid
O'-NO2 stretching [b]	957	Nitric acid
$v(O(1)–C(2)) + \delta(OH)$ [a]	962	2-Methoxyethanol
$v(C(3)–O(2))$ [a]	1020	2-Methoxyethanol
C-O stretching [c]	1030	Acetic acid
v1 s-stretching of $NO3^-$ [b]	1050	Nitric acid
$r(C(2)H2) + r(C(3)H2)$ [a]	1051	2-Methoxyethanol
$v(C(1)–O(1))$ [a]	1080	2-Methoxyethanol
$\gamma(CH_3)$ [a]	1097	2-Methoxyethanol
$t(C(3)H_2) + \delta(OH)$ [a]	1129	2-Methoxyethanol
$t(C(2)H_2) + t(C(3)H_2) + r(CH_3)$ [a]	1161	2-Methoxyethanol
$t(C(2)H_2) + t(C(3)H_2) + r(CH_3) + \delta(OH)$ [a]	1197	2-Methoxyethanol
$\omega(CH_2) + \delta(OH)$ [a]	1238	2-Methoxyethanol
$\omega(CH_2) + \delta(OH) + \gamma_s(CH_3)$ [a]	1286	2-Methoxyethanol
NO_2 s-stretching [b]	1309	Nitric acid
C-H bending [c]	1370, 1433	Acetic acid
$v(NO_2^+)$ [b]	1430	Nitric acid
$\gamma_{as}(CH_3) + \delta(CH_2)$ [a]	1454	2-Methoxyethanol
$\delta_{sci}(C(2)H_2) + \delta(CH_3)$ [a]	1475	2-Methoxyethanol
$2v\ NO_2$ bending o.p. [b]	1564	Nitric acid
Strongly hydrogen -bonded C=O group [c]	1665	Acetic acid
NO_2 a-stretching [b]	1682	Nitric acid
Weekly hydrogen- bonded and end C=O group [c]	1762	Acetic acid
$v_s(C(2)H_2)$ [a]	2726, 2774	2-Methoxyethanol
$v_s(CH_3)$ [a]	2831	2-Methoxyethanol
CH3 stretching [c]	2889	Acetic acid
$v_{as}(C(2)H2)$ [a]	2897	2-Methoxyethanol
$v_{as}(CH3)$ [a]	2938, 2989	2-Methoxyethanol
$v_{as}(C(3)H2)$, $v_s(C(3)H2)$ [a]	2947, 2950, 3000, 3035	2-Methoxyethanol
$v(OH)$ [a]	2990, 3600	Water
$v_{as}(OH)$ [a]	3440	2-Methoxyethanol
$v(OH)$ [a]	3552	Nitric acid

[a] Ref. [55], [b] Ref. [56]. [c] Ref. [57]

curves is similar, evidencing the $LaMnO_3$ phase formation above 650°C and the $EuMnO_3$ and $DyMnO_3$ phase formation above 750°C. It is important to keep in mind that these phase formation temperatures are in the same temperature interval of that reported by Kim and co-workers for the orthorhombic $YMnO_3$, which occurs between 650°C and 700°C [43].

3.2 Structural characterization

Figure 3 shows the grazing angle **X-ray** diffraction patterns of the as-prepared thin films, annealed at 650°C, 700°C, 750°C, 800°C, and 850°C, respectively, for $LaMnO_3$, and at 750°C, 800°C, and 850°C for both $EuMnO_3$ and $DyMnO_3$. The **X-ray** diffraction spectra of the $LaMnO_3$
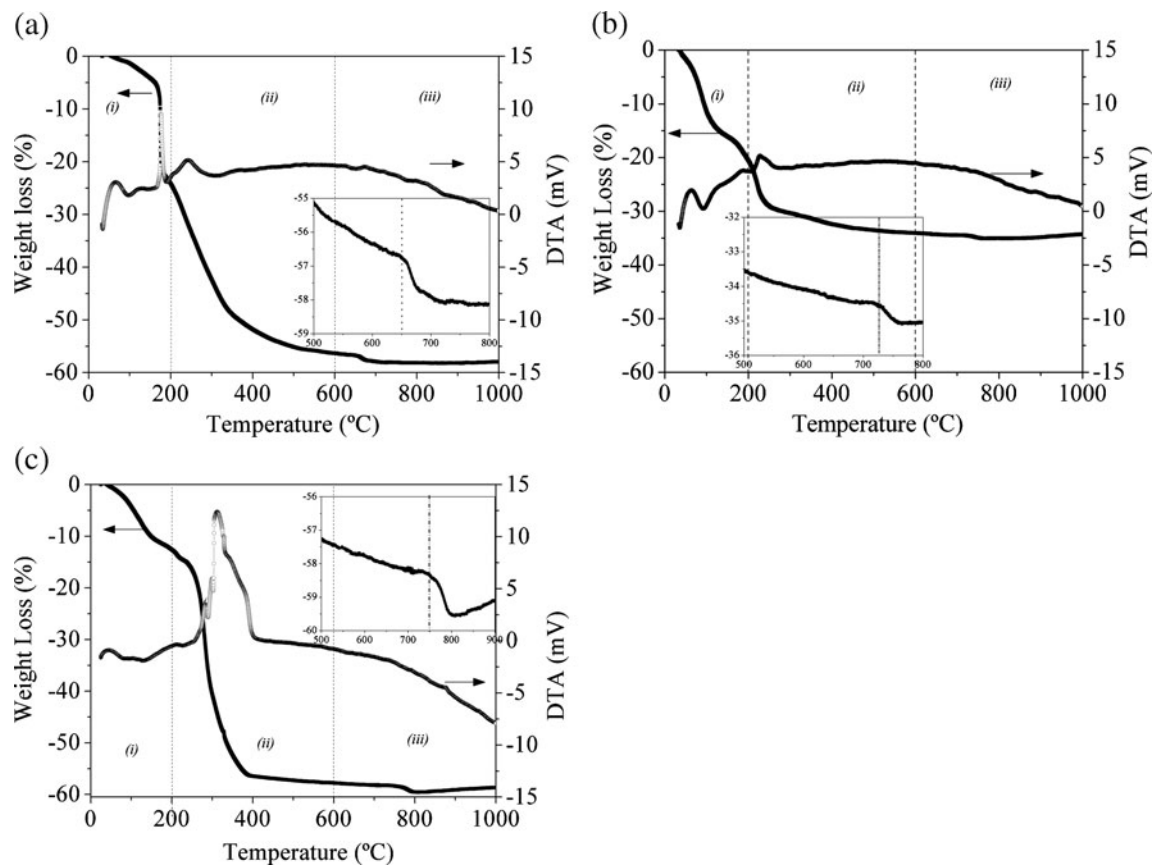
Fig. 2 Thermal decomposition curves of: (a) LaMnO$_3$, (b) EuMnO$_3$ and (c) DyMnO$_3$ solutions. Inset plots show the phase formation zone
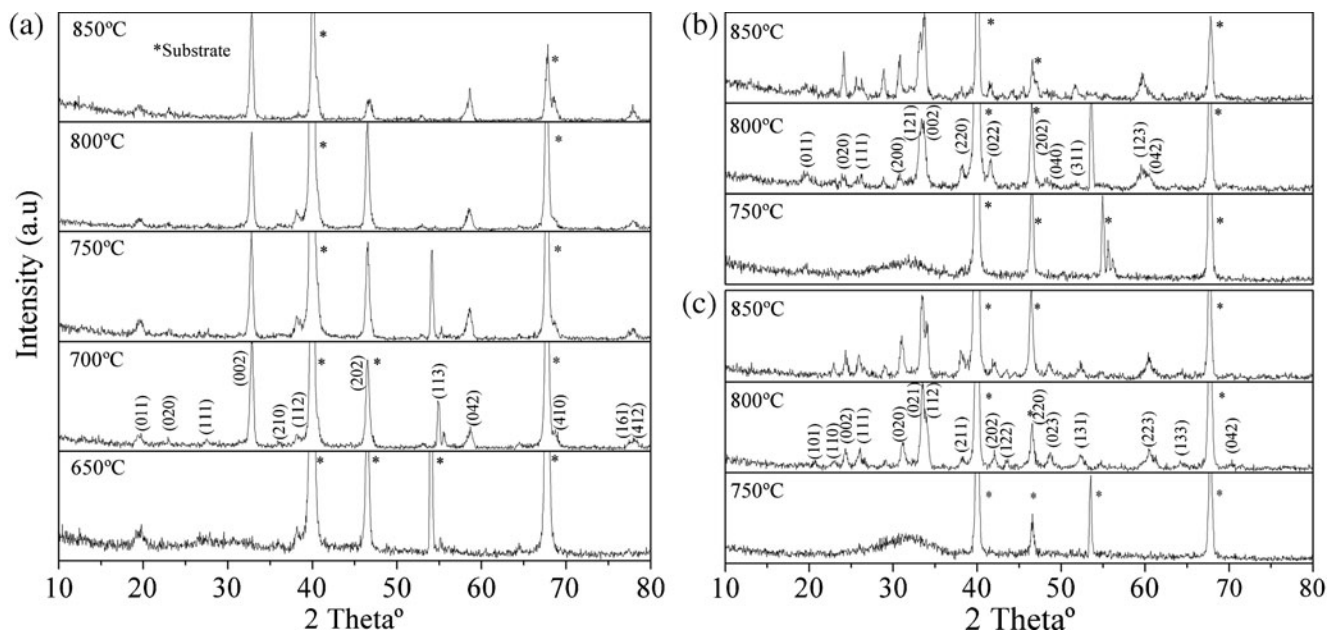

Fig. 3 Grazing angle X-ray diffraction patterns of: (a) LaMnO$_3$ films annealed at 650°C, 700°C, 750°C, 800°C and 850°C, (b) EuMnO$_3$ films annealed at 750°C, 800°C and 850°C, and (c) DyMnO$_3$ films annealed at 750°C, 800°C and 850°C

films, and both EuMnO$_3$ and DyMnO$_3$ films annealed at 650°C and 750°C, exhibit signatures arising from an amorphous phase, along with substrate diffraction peaks. Contrarily, the **X-ray** diffraction spectra of the LaMnO$_3$ films annealed above 650°C, and both EuMnO$_3$ and DyMnO$_3$ films annealed above 750°C, show a well defined peak structure that is characteristic of a single crystalline phase. All the diffraction peaks observed, excluding those coming from the substrate, are successfully assigned to a pure orthorhombic structure, with a space group *Pbnm*. Crystalline LaMnO$_3$ films annealed above 700°C show a (002) orientation, which is overlapped with the (121) one. On the other hand, as the annealed temperature increase towards 850°C, the (121) orientation of the EuMnO$_3$ films changes into (200), (020) and (002) orientations, while the (112) orientation of the DyMnO$_3$ remains unchanged (see Fig. 3(b) and (c)).

Figure 4 shows the Raman spectra of LaMnO$_3$, EuMnO$_3$ and DyMnO$_3$ crystalline thin films annealed at different temperatures, which were recorded at room temperature, in the 200 cm^{-1}–700 cm^{-1} frequency range. The parameters of the visible Raman modes (frequency, line width, and amplitude) were obtained from the best fit, using a sum of damped oscillator functions, and their frequencies are displayed in Table 2.

For orthorhombic LaMnO$_3$ thin films five main bands are observed, which are located at 221 cm^{-1}, 289 cm^{-1}, 426 cm^{-1}, 500 cm^{-1} and 630 cm^{-1}. A close look on Table 2 shows that the two higher frequency Raman frequencies shift towards higher values, and the corresponding widths are larger than the values observed for single crystals. This effect has also been observed in

LaMnO$_3$ thin films prepared by pulsed laser deposition method, which have been ascribed to a confinement effects [63]. The frequencies of the last four bands are in good agreement with those frequencies observed in single crystals for (i) out of phase MnO$_6$ *x*-rotations (284 cm^{-1}), (ii) out of phase MnO$_6$ bending mode (430 cm^{-1}), (iii) O (2) antistretching MnO$_6$ bending mode (490 cm^{-1}), and (iv) in plane O(2) stretching MnO$_6$ stretching mode (612 cm^{-1}) [64]. The 221 cm^{-1} Raman band is tentatively assigned to a strong lattice-substrate interaction, which decreases dramatically the frequency of the lattice mode located at 280 cm^{-1}, observed in the Raman spectra of single crystals. Although the analyzed samples exhibit crystalline phases, the Raman spectrum of the films annealed at the highest temperatures show the best defined band structure.

In the Raman spectra of EuMnO$_3$ and DyMnO$_3$ orthorhombic films several Raman bands are observed, which are located at 221 cm^{-1}, 356 cm^{-1}, 484 cm^{-1}, 501 cm^{-1}, 610 cm^{-1}, and 686 cm^{-1} and 218 cm^{-1}, 304 cm^{-1}, 389 cm^{-1}, 491 cm^{-1}, 515 cm^{-1}, 537 cm^{-1}, 622 cm^{-1} and 693 cm^{-1}, respectively. The band close to 690 cm^{-1}, observed in both EuMnO$_3$ and DyMnO$_3$ films, is not correlated with any of the Raman bands reported for both single crystals and ceramics [64]. It is not excluded that this relative high frequency band is a Raman activated infrared mode that appear due to a structural deformation of the molecular units. The Raman activation of infrared modes is not a hypothetic issue, it has been observed in other rare-earth manganites films by Prellier's group [65]. On the other hand, like in LaMnO$_3$ films, the lowest Raman band (located near 221 cm^{-1}) is assigned to a film-substrate
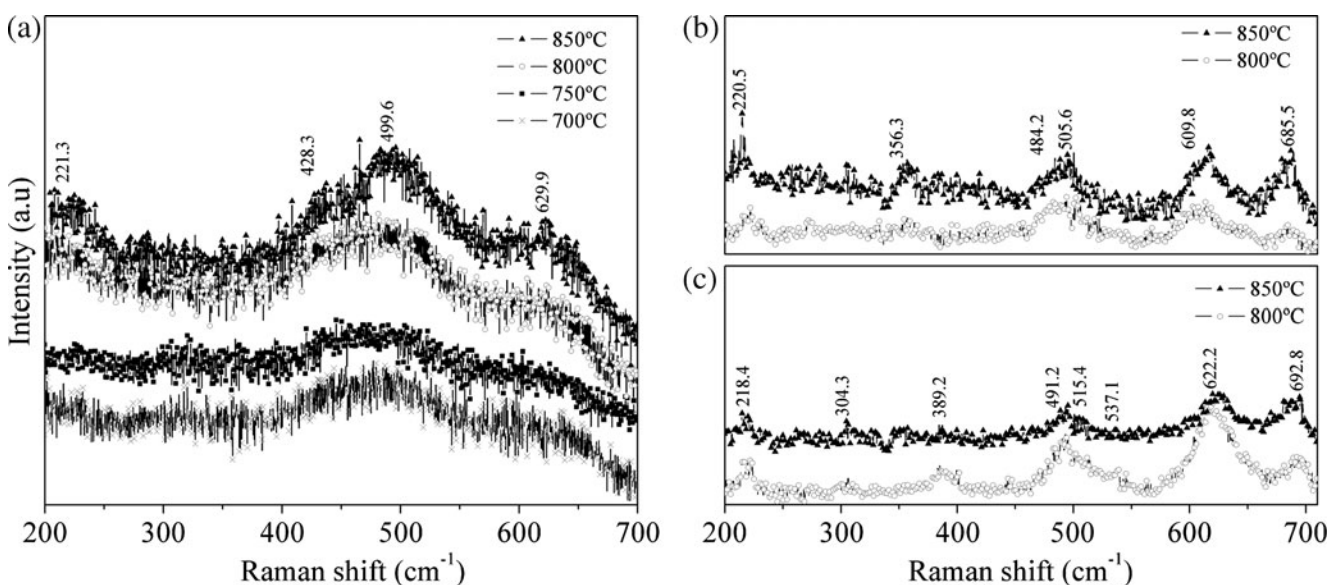

Fig. 4 Room temperature Raman Spectra of: (a) LaMnO$_3$, (b) EuMnO$_3$ and (a) DyMnO$_3$ thin films annealed at different temperatures

Table 2 LaMnO₃, EuMnO₃, and DyMnO₃ experimental and single crystals Raman bands reported at RT [d]

Activation mode	Main atomic motions	LaMnO$_3$ single crystals	LaMnO$_3$ experimental	EuMnO$_3$ single crystals	EuMnO$_3$ experimental	DyMnO$_3$ single crystals	DyMnO$_3$ experimental
$A_g(1) \rightarrow A_g(3)$	O2 antistretching $\rightarrow$ MnO$_6$ bending	490.7	499.6	505.6	501.0	513.4	515.4
$A_g(3) \rightarrow A_g(1)$	O2 antistretching $\rightarrow$ MnO$_6$ bending	–	–	479.0	484.2	492.1	491.2
$A_g(4)$	Out of phase MnO6 x-rotations	283.6	289.4	360.8	356.3	386.0	389.2
$A_g(7) \rightarrow A_g(2)$	O1(x) $\rightarrow$ in-phase MnO$_6$ y-rotations	–	–	–	–	319.5	304.3
$B_{2g}(1)$	in–plane O2 stretching	612.3	629.9	609.5	609.8	613.5	622.2
$B_{2g}(2)$	In-phase O2 *scissorslike*	–	–	–	–	533.6	537.2
$B_{2g}(3)$	Out-of-phase MnO$_6$ bending	430.0	426.3	–	–	–	–
Unknown	–	–	221.3	–	220.5	–	218.5
Unknown	–	–	–	–	685.5	–	692.8

[d] Ref. [64]

interaction. A summarized of these manganites modes is shown in Table 2.

The results obtained from both X-ray diffraction and Raman spectroscopy clearly confirm the P*bnm* orthorhombic structure of the as-prepared films, annealed above 650°C for LaMnO₃, and above 750°C for both EuMnO₃ and DyMnO₃ thin films. The next two sections will be addressed to the study of both microstructure and magnetic response of the as-processed films, considering only those with an evident orthorhombic phase formation.

3.3 Microstructure characterization of the films

Scanning electron microscopy (SEM) plan-view images of the LaMnO₃ films annealed at 700°C, 800°C and 850°C, and both EuMnO₃ and DyMnO₃ thin films annealed at 750°C, 800°C and 850°C, are show in Fig. 5.

LaMnO₃ film annealed at 700°C exhibits a relative smooth surface, with an incipient grain growth (see Fig. 5 (a)). As the annealing temperature increases above 700°C (Fig. 5(b), and (c)), there is an improvement in the grain structure of the films. This improvement results in a well-defined grain boundary and a mean grain size of 50 nm in the LaMnO₃ film annealed at 850°C.

SEM plan-view images of the EuMnO₃ show a visible underground grain growth in the film annealed at 750°C, as shown in Fig. 5(d). There is an increase in the grain growth as the annealing temperature **increases;** showing a defined grain structure for the films annealed at 800°C and 850°C (see Fig. 5(e) and (f)). The EuMnO₃ thin film annealed at 800°C reveals a large grain structure with a diameter of ~400 nm. These large grains are composed by small grains, with an average size of ~50 nm. On the other hand,

the film annealed at 850°C shows a sponge-type surface that could be assigned to grains rearrangement and faster nucleation process, which takes place during the crystallization process at high temperature [66].

SEM images displayed in Fig. 5(g) show an undefined structure for the DyMnO₃ films annealed at 750°C, whereas the films annealed at 800°C (Fig. 5(h)) and 850°C (Fig. 5 (i)) show a grain cluster size of ~2000 nm, and sponge-type surfaces, which are typical of an accelerated grain growth process.

As the preparation conditions were maintained for all films, the thickness is practically equal for all the as-processed films, taking the mean value 250 nm. Figure 6 show a representative SEM cross-section image for all the films, recorded on the EuMnO₃ film annealed at 800°C. Energy dispersive X-ray spectroscopy analysis of this film exhibits peaks corresponding to the EuMnO₃ compound, along with a carbon peak, arising from the SEM carbon glue used, and two other peaks, arising from silicon and platinum substrate.

Tapping mode atomic force microscopy measurements were carried out in order to confirm the surface morphology results obtained by the SEM analysis. Figure 7 (a), (b) and (c) show the AFM images **for** the LaMnO₃ films annealed at 700°C, 800°C and 850°C**. They reveal** a homogeneous grain growth **up to** ~210 nm, which is in good agreement with those observed by SEM.

Atomic force **microscopy images** of the EuMnO₃ films annealed at 750°C, 800°C and 850°C are displayed in Fig. 7(d), (e) and (f), respectively. The film annealed at 750°C shows a smooth microstructure, whereas those annealed at 800°C and 850°C reveal a well-defined structure and an average grain size of ~420 nm. Identical grain size values were obtained from both AFM and SEM

Fig. 5 Scanning electron microscopy images of LaMnO$_3$ thin films annealed at: (**a**) 700°C, (**b**) 800°C and (**c**) 850°C, EuMnO$_3$ thin films annealed at: (**d**) 700°C, (**e**) 800°C and (**f**) 850°C and DyMnO$_3$ thin films annealed at: (**g**) 750°C, (**h**) 800°C and (**i**) 850°C
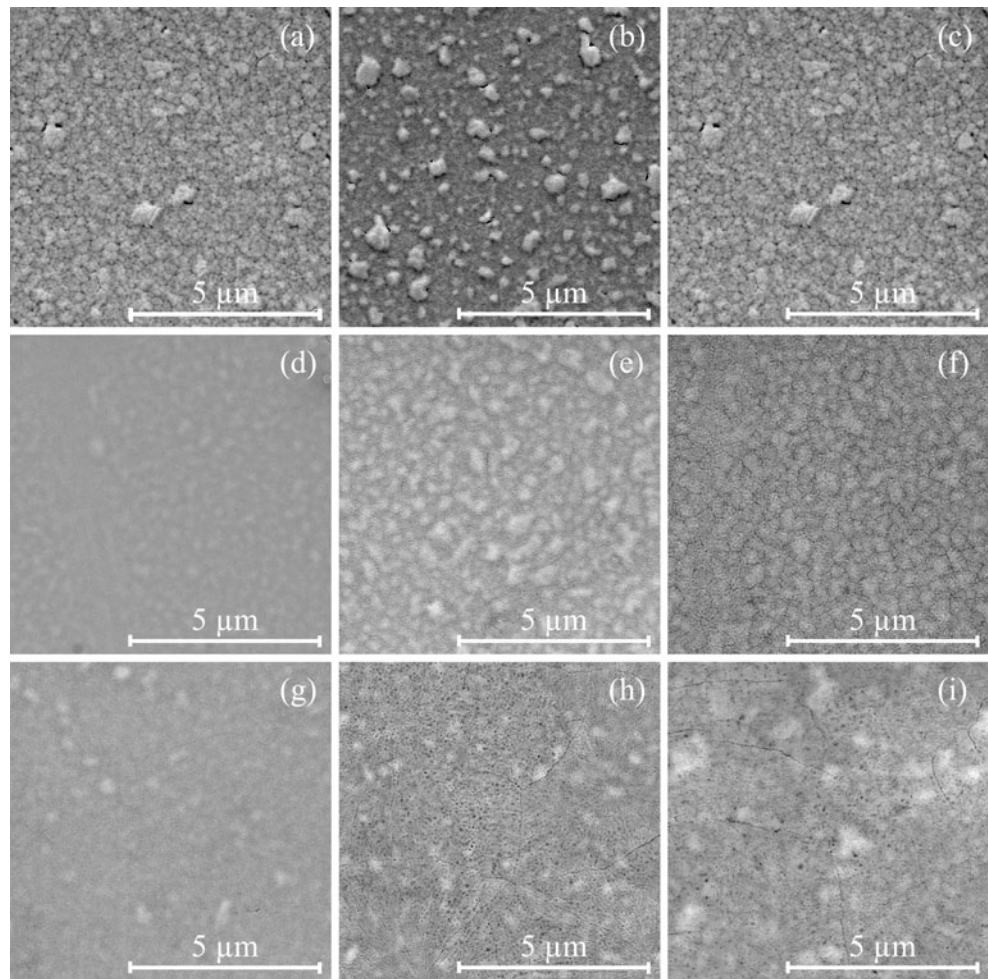
techniques. However, the sponge-type surface observed in the EuMnO$_3$ film annealed at 850°C by SEM analysis is not confirmed by the AFM technique.

The AFM images recorded in the DyMnO$_3$ thin films annealed at 750°C show also smooth microstructure, as shown in Fig. 7(g). Contrarily, the films annealed at both
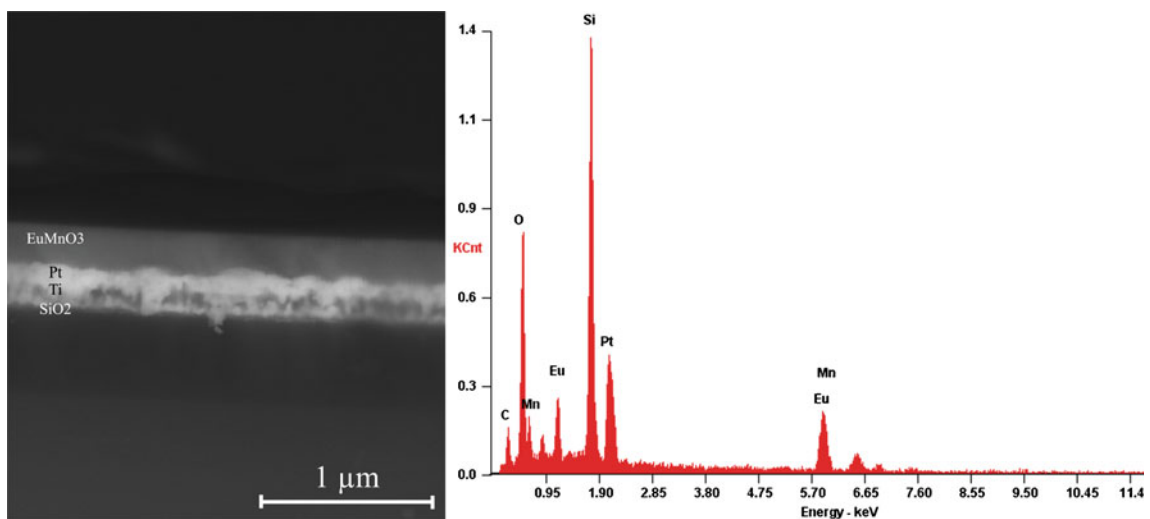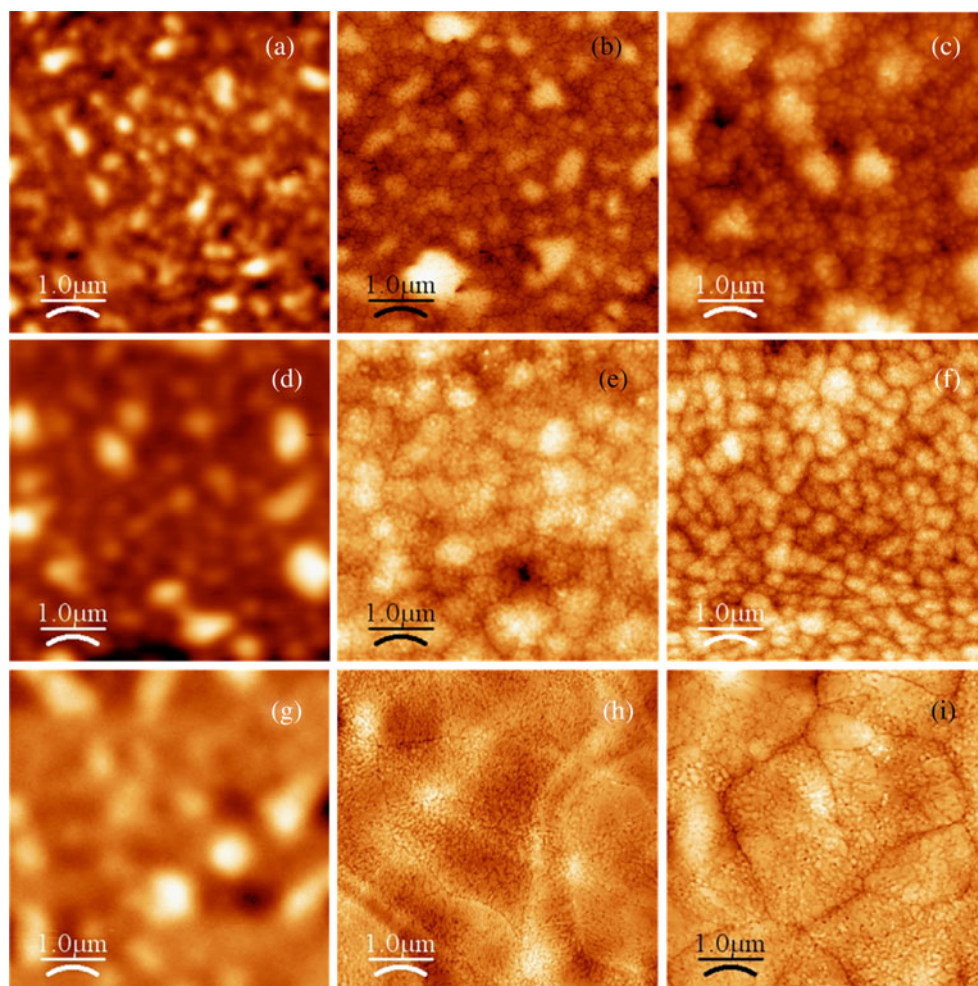

Fig. 6 (**a**) Representative cross-section backscattering scanning electron microscopy image of all the thin films and (**b**) EDS analysis of this film (EuMnO$_3$ annealed at 800°C)

Fig. 7 AFM images of LaMnO$_3$ thin films annealed at: (**a**) 700°C, (**b**) 800°C and (**c**) 850°C, EuMnO$_3$ thin films annealed at: (**d**) 700°C, (**e**) 800°C and (**f**) 850°C and DyMnO$_3$ thin films annealed at: (**g**) 750°C, (**h**) 800°C and (**i**) 850°C

800°C and 850°C (Fig. 7(h) and (i)) show a well-defined grain cluster structure with approximately 2000 nm. These large grain clusters are actually composed by several small grains, with a mean grain size of ~75 nm. The typical sponge-type surface obtained in the DyMnO$_3$ thin films annealed at 800°C and 850°C by SEM analysis is not observed in the AFM images.

It is clear from the AFM analysis that all samples exhibit small surface porosity. The largest grain growth, the surface shape, and the porosity observed by AFM analysis also reveal an accelerate nucleation process, which take place at higher annealing temperatures (above 750°C) [66], as those obtained for the DyMnO$_3$ manganites annealed at both 800°C and 850°C.

3.4 Magnetic film characterization

Figures 8 (a–c) show the induced magnetization of LaMnO$_3$, EuMnO$_3$ and DyMnO$_3$ thin films annealed at 800°C, while the magnetic contribution of the substrate (pre-heated at 800°C) is shown in Fig. 8(d). The magnetic

response of the substrate was expected to be diamagnetic, due to the higher contribution of the silicon and silicon dioxide layers; however, the overall magnetic response was positive, small and practically unchangeable with the temperature. It is associated to paramagnetic response of the platinum and titanium layers and also to the impurities present in the silicon layer. For magnetic parameters evaluation analysis, this contribution was subtracted for the overall magnetic response of the films.

The temperature dependence of the ZFC induced magnetization of the LaMnO$_3$ film exhibits broad anomalies at 41 K and 211 K (Fig. 8(a)). The higher one is likely associated with the paramagnetic-antiferromagnetic phase transition, occurring at 140 K in high quality single crystals and ceramics [46]. The large increase of the phase transition temperature could have origin in the non-stoichiometry of the compound. It is well known that La$_{1-\delta}$MnO$_3$ exhibit an up-shift of the phase transition temperature, and a pronounced ferromagnetic character, arising from the canting of the antiferromagnetic arrangement of spins [50, 67]. Looking at the magnetization measured in field cooling

Fig. 8 Temperature dependence of the field cooling and zero field cooling magnetization of: (**a**) LaMnO$_3$ films, (**b**) EuMnO$_3$ films, (**c**) DyMnO$_3$ films and (**d**) platinum substrate annealed at 800°C
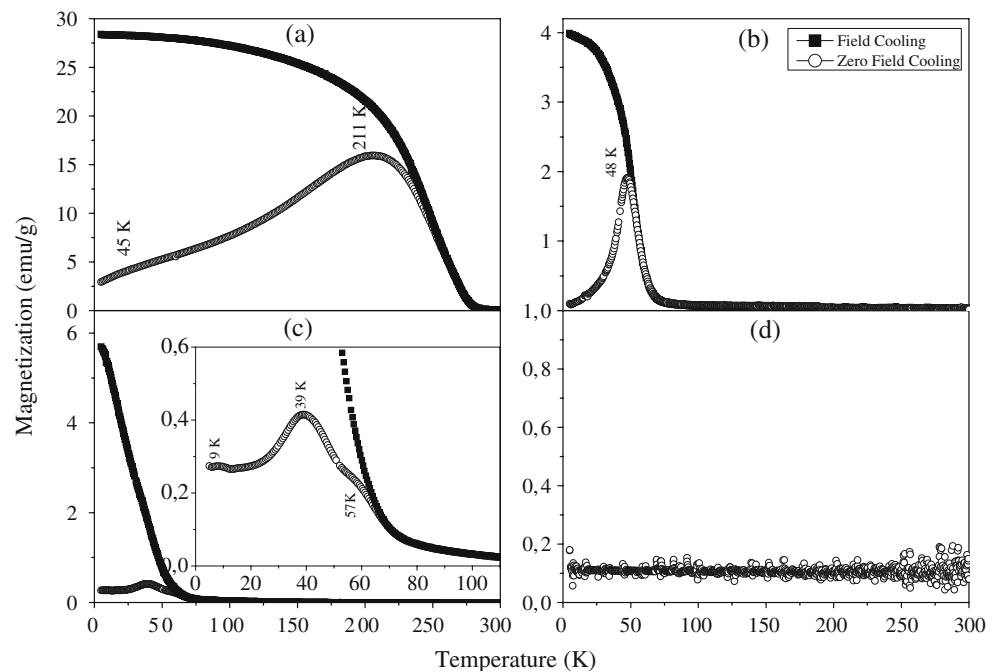
conditions, a clear ferromagnetic character of our sample is evidenced. So, we attribute the broad anomaly at 211 K to a non-stoichiometry in the sample. The shoulder in the magnetization at 41 K might be associated with ferromagnetic domains re-arrangements.

The temperature dependence of the EuMnO$_3$ film magnetization at zero field cooled and field cooled is shown in Fig. 8(b). It is observed a remarkable anomaly at 46 K in the magnetization as a function of temperature, measured in zero field cooling conditions, which corresponds to the transition from the paramagnetic into the incommensurate antiferromagnetic phases. This result is in good agreement with the early report for EuMnO$_3$ by Pauthenet and Veyret (~45 K) [51]. Moreover, the transition from the incommensurate antiferromagnetic phase to the canted A-type antiferromagnetic one, reported for both single crystals and ceramics, is not detected by any anomaly of the magnetization as a function of temperature.

Figure 8(c) shows the ZFC and FC temperature dependence of the magnetization of DyMnO$_3$ film. Anomalies at 9 K, 39 K, and 57 K are observed in the ZFC curve. These anomalies are also observed in the magnetization of single crystal, but at lowest temperatures [4, 10]. Since DyMnO$_3$ is located near the structural phase boundary, it exhibits a complex low temperature magnetic state and magnetoelectric properties [4]. As aforesaid, it is reasonable to think that several parameters (among them, substrate clamping, oxygen vacancies, film stoichiometry, film grain size, and impurities) could modify the dysprosium manganite octahedron, and consequently the Mn-O-Mn bond angle. This octahedron modification could

explain the up-shift of the transition temperatures. On the other hand, the lowest temperature transition is associated with a ordering of the Dy^{3+} magnetic momenta, as reported by Kimura and co-workers [10].

4 Conclusions

High-quality manganite thin films were prepared by a general and novel chemical solution deposition route. For this purpose, stable and reproducible LaMnO$_3$, EuMnO$_3$ and DyMnO$_3$ precursor solutions were prepared by a nitric/acetic acids and 2-methoxyethanol and characterized by Raman technique. Moreover, the solution decomposition process and phase formation temperature were analyzed by TG and DTA techniques. The pre-selected solutions were deposited on Pt/TiO$_2$/SiO$_2$/Si substrate by a spin-coating method and the resulting films were annealed between 600°C and 850°C. The structural analysis show the formation of a pure orthorhombic phase for LaMnO$_3$ films annealed above 650°C and above 750°C for both EuMnO$_3$ and DyMnO$_3$ films. The morphology analysis reveals the formation of a ~50 nm grain in all the LaMnO$_3$ crystalline films, an increase of the grain size up to 420 nm with the increase of the annealing temperature in EuMnO$_3$ films and the formation of large cluster with ~2000 nm in DyMnO$_3$ thin films annealed at both 800°C and 850°C. Structural and morphological results also suggest that an increase in the annealing temperature improves both the film crystallization process and preferential orientation. The films magnetic study below room temperature, at field cooling

and zero field cooling, reveals the clear magnetic behavior of the as-prepared samples, which are in agreement with those reported for lanthanum, europium and dysprosium manganite single crystals and ceramics.

References

1. H. Schmid, Ferroelectrics **162**, 317–338 (1994)
2. S. Jin, T.H. Tiefel, M. McCormack, R.A. Fastnacht, R. Ramesh, L.H. Chen, Science **264**, 413–415 (1994)
3. Y. Tokura, Y. Tomioka, J Magn Magn Mater **200**, 1–23 (1999)
4. T. Goto, T. Kimura, G. Lawes, A.P. Ramirez, Y. Tokura, Phys Rev Lett **92**, 257201–257204 (2004)
5. M. Grizalez, E. Delgado, M.E. Gómez, P. Prieto, Phys Status Solidi C **4**, 4203–4208 (2007)
6. R. Ramesh, N.A. Spaldin, Nat Mater **6**, 21–29 (2007)
7. S. Lee, A. Pirogov, M. Kang, K.-H. Jang, M. Yonemura, T. Kamiyama, S.-W. Cheong, F. Gozzo, N. Shin, H. Kimura, Y. Noda, J.-G. Park, Nat Lett **451**, 805–808 (2008)
8. M.A. Gilleo, Acta Crystallogr **10**, 161–166 (1957)
9. H. Yakel, W. Koehler, E. Bertaut, F. Forrat, Acta Crystallogr **16**, 957–962 (1963)
10. T. Kimura, G. Lawes, T. Goto, Y. Tokura, A.P. Ramirez, Phys. Rev. B, **71**, 224425_1-13 (2005)
11. J.A. Alonso, M.J. Martínez-Lopez, M.T. Casais, M.T. Fernández-Diaz, Inorg Chem **39**, 917–923 (2000)
12. G. Maris, V. Volotchaev, T.T.M. Palstra, New J. Phys., **6**, 153_1-11 (2004)
13. W.S. Choi, D.G. Kim, S.S.A. Seo, S.J. Moon, D. Lee, J. H. Lee, H.S. Lee, D.-Y. Cho, Y.S. Lee, P. Murugavel, J. Yu, T.W. Noh, Phys. Rev. B, **77**, 045137_1-7 (2008)
14. D. Lee, J.H. Lee, P. Murugavel, S.Y. Jang, T.W. Noh, Y. Jo, M.H. Jung, Y.D. Ko, J.S. Chung, Appl. Phys. Lett., **90**, 182504_1-3 (2007)
15. E.E. Kaul, N. Haberkorn, J. Guimpel, Appl Surf Sci **254**, 160–163 (2007)
16. K. Suzuki, K. Nishizawa, T. Miki, K. Kato, J Cryst Growth **237**, 482–486 (2002)
17. W. Prellier, M.P. Singh, P. Murugavel, J Phys-Condens Matter **17**, R803–R832 (2005)
18. G. Lalitha, P. Venugopal Reddy, J Magn Magn Mater **320**, 754–759 (2008)
19. Y. Tadokoro, Y.J. Shan, T. Nakamura, S. Nakamura, Sol Stat Ionics **108**, 261–267 (1998)
20. Th. Lottermoser, M. Fiebig, D. Fröhlich, St. Leute, K. Kohn, J. Magn. Magn. Mater. **226**, 1131–1133 (2001)
21. F.S. Galasso, *Structure Properties and Preparation of Perovskite-Type Compounds* (Pergamon, Oxford, 1968)
22. P.A. Salvador, T.D. Doan, B. Mercey, B. Raveau, Chem Mater **10**, 2592–2595 (1998)
23. A. Muñoz, J.A. Alonso, M.J. Martínez-Lope, M.T. Casaís, J.L. Martínez, M.T. Fernández-Díaz, Chem Mater **13**, 1497–1505 (2001)
24. O. Yu, Gorbenko, S.V. Samoilenkov, I.E. Graboy, A.R. Kaul, Chem Mater **14**, 4026–4043 (2002)
25. M.R. Lees, J. Barratt, G. Balakrishnan, D.M. Paul, Phys Rev B **52**, R14303–R14307 (1995)
26. Y. Tomioka, A. Asamitsu, Y. Morotomo, Y. Tokura, J Phys Soc Jpn **64**, 3626–3630 (1995)
27. S.Y. Prilipko, V.M. Timchenko, G.Y. Akimov, V.I. Tkach, Powder Metall Met C+ **47**, 5–6 (2008)
28. J. Agostinho Moreira, A. Almeida, W.S. Ferreira, M.R. Chaves, J.B. Oliveira, J.M. Machado da Silva, M.A. Sá, S.M.F. Vilela, P.B. Tavares, Structural, thermodynamic, dielectric and magnetic properties of $Eu_{0.8}Y_{0.2}MnO_3$ ceramics prepared by urea sol-gel combustion method. J. Mat. Sci., (Submmited 2009); W.S. Ferreira, et. al., Phys. Rev. B, **79**, 54303_1–10 (2009)
29. X. Martí, F. Sánchez, D. Hrabovsky, J. Fontcuberta, V. Laukhin, V. Skumryev, M.V. García-Cuenca, C. Ferrater, M. Varela, U. Lüders, J.F. Bobo, S. Estradé, J. Arbiol, F. Peiró, J Cryst Growth **299**, 288–294 (2007)
30. K.X. Jin, S.G. Zhao, X.Y. Tan, C.L. Chen, X.W. Jia, Appl Phys A Mater **95**, 789–792 (2009)
31. H.N. Lee, Y.T. Kim, Y.K. Park, Appl Phys Lett **74**, 3887–3889 (1999)
32. Y.T. Kim, I.S. Kim, S. Kim II, D.C.H. Yoo, J.Y. Lee, J Appl Phys **94**, 4859–4862 (2003)
33. A. Posadas, J.B. Yau, C.H. Ahn, J. Han, S. Gariglio, K. Johnston, K.M. Rabe, J.B. Neaton, Appl. Phys. Lett. **87**, 171915_1-3 (2005)
34. S. Imada, S. Shouriki, E. Tokumitsu, H. Ishiwara, Jpn J Appl Phys **37**, 6497–6501 (1998)
35. S. Imada, T. Kuraoka, E. Tokumitsu, H. Ishiwara, Jpn J Appl Phys **40**, 666–671 (2001)
36. A.A. Bosak, A.A. Kamenev, I.E. Graboy, S.V. Antonov, G.O. Yu, A.R. Kaul, C. Dubourdieu, J.P. Senateur, V.L. Svechnikov, H.W. Zandbergen, B. Hollaender, Thin Solid Films **400**, 149–153 (2001)
37. W.C. Yi, J.S. Choe, C.R. Moon, S.I. Kwun, J.G. Yoon, Appl Phys Lett **73**, 903–905 (1998)
38. H. Kitahata, K. Tadanaga, T. Minami, N. Fujimura, T. Ito, Appl Phys Lett **75**, 719–721 (1999)
39. H. Kitahata, K. Tadanaga, T. Minami, N. Fujimura, T. Ito, J Sol-Gel Sci Technol **19**, 589–593 (2000)
40. K. Tadanaga, H. Kitahata, T. Minami, N. Fujimura, T. Ito, J Sol-Gel Sci Technol **13**, 903–907 (1998)
41. H. Kitahata, K. Tadanaga, T. Minami, N. Fujimura, T. Ito, J Am Ceram Soc **81**, 357–1360 (1998)
42. G. Teowee, K.C. McCarthy, F.S. McCarthy, T.J. Bukowski, D.G. Davis Jr., D.R. Uhlmann, J Sol-Gel Sci Technol **13**, 899–902 (1998)
43. K.T. Kim, C.I. Kim, J Eur Ceram Soc **24**, 2613–2617 (2004)
44. X. Zhu, D. Shi, L. Zhang, Y. Sun, W. Song, L. Wang, T.M. Silver, S. Dou, J Alloys Compd **459**, 83–86 (2008)
45. Y. Shimizu, T. Murata, J Am Ceram Soc **80**, 2702–2704 (1997)
46. C. Ritter, M.R. Ibarra, J.M. De Teresa, P.A. Algarabel, C. Marquina, J. Blasco, J. García, S. Oseroff, S.-W. Cheong, Phys Rev B **56**, 8902–8911 (1997)
47. G.L. Liu, J.S. Zhou, J.B. Goodenough, Phys. Rev. B **64**, 144414_1-7 (2001)
48. H.C. Ku, C.T. Chen, B.N. Lin, J Magn Magn Mater **272–276**, 85–87 (2004)
49. C. Papastaikoudis, E. Syskakis, J Magn Magn Mater **272–276**, 444–445 (2004)
50. C. Krishnamoorthy, K. Sethupathi, V. Sankaranarayanan, R. Nirmala, S.K. Malik, J Alloys Compd **438**, 1–7 (2007)
51. R. Pauthenet, C. Veyret, J Phys **31**, 65–72 (1970). in Frances
52. Y.M. Mukovskii, G. Hilscher, H. Michor, A.M. Ionov, J Appl Phys **83**, 7163–7165 (1998)
53. A.M. Kadomtsev, Y.F. Popov, G.P. Vorob'ev, V.Y. Ivanov, A.A. Mukhin, A.M. Balbashov, JETP Lett **81**, 590–593 (2005)
54. M. Tokunage, I. Katakura, Y. Yamasaki, Y. Onose, F. Tokura, J. Phys-Conf. Series **150**, 042212_1-4 (2009)
55. A.M. Amorim da Costa, A.S.R. Duarte, A.M. Amado, Vib Spectrosc **42**, 302–308 (2006)

56. H. Lucas, J.P. Petitet, J Phys Chem A **103**, 8952–8958 (1999)
57. T. Nakabayashi, K. Kosugi, N. Nishi, J Phys Chem A **103**, 8595–8603 (1999)
58. T. Kubota, O. Tochiyama, K. Tanaka, Y. Niibori, Radiochim Acta **88**, 579–582 (2000)
59. J. Moreau, E. Guillon, P. Aplincourt, J.C. Pierrard, J. Rimbault, M. Port, M. Aplincourt, Eur J Inorg Chem **16**, 3007–3020 (2003)
60. T. Sasaki, S. Kubo, T. Kobayashi, I. Tagaki, H. Moriyama, J Nucl Sci Technol **42**, 724–731 (2005)
61. R. Hammami, S.B. Aïssa, H. Batis, Appl Catal A Gen **353**, 145–153 (2009)
62. Y. Li, L. Xue, L. Fan, Y. Yan, J Alloys Compd **478**, 493–497 (2009)
63. A. Dubey, V.G. Sathe, J. Phys-Condens. Mat. **19**, 346232_1-10 (2007)
64. M.N. Iliev, M.V. Abrashev, J. Laverdière, S. Jandl, M.M. Gospodinov, Y.Q. Wang, Y.Y. Sun, Phys. Rev. B **73**, 064302_1-6 (2006)
65. A. Antonakos, D. Palles, E. Liarokapis, M. Filippi, W. Prellier, J. Appl. Phys. **104**, 063508_1-10 (2008)
66. M.W. Barsoum, *Fundamentals of Ceramics* (Taylor & Francis, New York, 2002)
67. P. Raychaudhuri, C. Mitra, J Appl Phys **93**, 8328–8330 (2003)